https://doi.org/10.5194/essd-2026-261
Preprint. Discussion started: 28 April 2026

Open Access Earth System Science Data Discussions

A global high-resolution temperature and salinity reconstruction by spatiotemporal multiscale correlations and dynamic height constraints

Haowen Wu[1], Wei Li[1*], Hong Li[1*], Guijun Han[1], Gongfu Zhou[1], Hanyu Liu[1], Lige Cao[1], Qingyu Zheng[1]

[1]Tianjin Key Laboratory for Marine Environmental Research and Service, School of Marine Science and Technology, Tianjin University, Tianjin, China

Correspondence to: Wei Li (liwei1978@tju.edu.cn), Hong Li (hongli@tju.edu.cn)

Abstract. High-resolution temperature and salinity (*T* & *S*) gridded datasets are essential for exploring large and mesoscale ocean phenomena. In this study, a global, weekly *T* & *S* gridded dataset with a horizontal resolution of 1/4° and a depth range of 0–1500 m from 2005 to 2023 is reconstructed using a four-dimensional multigrid analysis (4D-MGA) framework. With minimal prior statistical assumptions, the 4D-MGA efficiently extracts information from in-situ *T* & *S* profiles and satellite-observed sea level anomalies by integrating multiscale spatiotemporal correlation and physical constraints. The results show that the 4D-MGA product successfully delivers a credible, high-resolution analysis that combines robustness with reliable mesoscale information. Specifically, our product exhibits a lower root mean square error and excellent unbiased performance on a global scale when compared with the ARMOR3D product and the GLORYS reanalysis. http The product is then applied to investigate the linear trends of geostrophic transport within five key sections in WBCs. The 4D-MGA product is a subset of the high-resolution, objective analysis, gridded dataset for oceans, and it has the potential to advance our understanding of ocean dynamics and climate change. The weekly reconstructed dataset (4D-MGA) is freely available at https://doi.org/10.5281/zenodo.19378150.

1 Introduction

Temperature and salinity (*T* & *S*) are recognised as the two fundamental factors in the physical oceanography (Talley et al., 2011). Three-dimensional (3D) gridded *T* & *S* fields play a crucial role in studying multi-scale ocean dynamics (e.g., Zhang et al., 2014; Li et al., 2022; Miyaji et al., 2025; Zhou et al., 2025), optimizing ocean observations (e.g. Tan et al., 2023, 2025; Garcia et al., 2024; Reagan et al., 2024b), evaluating model performance (e.g., Tang et al., 2003; Matei et al., 2012; Polkova et al., 2023), as well as investigating climate change (e.g. Lyman and Johnson, 2014; Ishii et al., 2017; Bagnell and DeVries, 2021; Liang et al., 2021; Liu et al., 2026; Pan et al., 2026). The reconstruction of a global, high-quality 3D *T* & *S* fields remains a fundamental pursuit in the relevant literature.

Nowadays, three distinct types of 3D *T* & *S* products have been identified, namely the objective analysis, the reanalysis, and the artificial intelligence (AI) based products, according to the historical development of the subject. Objective analysis products were established through the spatiotemporal correlation of error distributions between observations and background fields (Roemmich and Gilson, 2009; Guinehut et al., 2012; Good et al., 2013; Gaillard et al., 2016; Cheng and Zhu, 2016; Li et al., 2017; Zhou et al., 2023). Reanalysis products utilize ocean numerical models to supply background information, and combine assimilation methods to link the observations and models to produce dynamically consistent *T* & *S* analyses (Forget et al., 2015; Chamberlain et al., 2021; Lellouche et al., 2021; Chepurin et al., 2025; De Boisseson et al., 2025). AI products have grown in recent years. They are based on learning the representative correlations among multiple input variables (e.g., Su et al., 2020; Tian et al., 2022; Zhu et al., 2025; Wang et al., 2025).

Each product possesses advantages and disadvantages. Reanalysis products are capable of representing continuous dynamical evolution with fine-scale structures (e.g., Mason et al., 2019; Castillo-Trujillo et al., 2023; El Aouni et al., 2025). Nonetheless, the model errors and parameterisation uncertainties will give rise to unrealistic results (e.g., Schneider et al., 2013; Paul et al., 2025). AI-based products offer powerful nonlinear fitting capabilities, but there are limitations in interpretability, the risk of perpetuating biases, and errors present in training data (Gray et al., 2024; Nunziante et al., 2025). In contrast, objective analysis products show lower performance in continuity and resolution, but can provide the most reliable representation of observations, with minimal errors (Chang et al., 2014; Carton et al., 2019). What's more, the heavy reliance on observations ensures a greater degree of determinism. They are often regarded as a reference benchmark for evaluations (e.g., Szekely, 2022; Cao et al., 2026), though their quality is dependent on the quantity and distribution of observations.

At present, the distribution of the in-situ *T* & *S* observations is uneven in terms of both space and time. Even for the largest global observation system, the spatial resolution of Argo is only ~3°×3° (Argo, 2026). Therefore, the present objective analysis products remain limited in capturing mesoscale signals due to their relatively low horizontal resolution (1°×1°) (e.g., Roemmich and Gilson, 2009; Gaillard et al., 2016; Cheng and Zhu, 2016; Li et al., 2017), which hampers our understanding of the multi-scale oceanic dynamic processes. On the other hand, the satellite-based products feature relatively high spatiotemporal resolutions (e.g. Donlon et al., 2012; AVISO/DUACS, 2024), while they cannot provide subsurface information. It is still challenging to combine in-situ and satellite observations in objective analysis to create global, high-quality and high-resolution 3D gridded *T* & *S* fields.

The issue under consideration is the challenge of separating multi-scale superimposed signals and leverage the spatiotemporal continuity and multivariate physical linkages in most objective analysis methods (e.g., Paris et al., 2002; Gray and Riser, 2015). The four-dimensional multigrid analysis (4D-MGA; Zhou et al., 2023, Wu et al., 2026b) method is an excellent candidate for simultaneously addressing these challenges. The 4D-MGA framework features spatiotemporal evolution constraints and deterministic physical links without relying on prior statistical assumptions. Thus, error signals in *T* & *S* fields are progressively distilled from large to small scales. Based on these advantages, 4D-MGA has been successfully used in reconstructing 3D gridded *T* & *S* fields in a regional ocean with a powerful ability to capture mesoscale signals (e.g., Zhou et al., 2023). Now it is time for us to use this excellent method to reconstruct a global high-resolution 3D gridded *T* & *S* field.

This study constructs a 1/4° global subsurface (0–1500 m) *T* & *S* gridded dataset from 2005–2023 based on the 4D-MGA method. A comprehensive evaluation of the dataset is conducted. Furthermore, the detailed 3D structure and long-term trends of the transport of the western boundary currents (WBCs) were also investigated.

The remainder of this paper is organized as follows. Section 2 introduces the datasets and the 4D-MGA method employed in this study. The overall performance of our product is introduced in Section 3. As an application of the 4D-MGA product, the linear trends in geostrophic transports in WBCs are discussed in Section 4. Data availability is described in Section 5. Sections 6 and 7 provide conclusion and discussion.

2 Data and Methods

2.1 Data

2.1.1 Background Field

Weekly background fields of *T*, *S* and sea level anomaly (SLA) are required as prior inputs for the 4D-MGA. The *T/S* background fields are derived from the high-resolution (1/4°) World Ocean Atlas 2023 (WOA23; Reagan et al., 2024a). To match our study period, we merged the available WOA23 decadal monthly fields (2005–2014 and 2015–2022) via time-span weighted averaging to generate a representative climatology. The SLA climatology was computed from daily CMEMS Level-4 gridded SLA data (https://doi.org/10.48670/moi-00148) over the same period. All monthly climatological fields were linearly interpolated to the weekly analysis times, corresponding to the 4D-MGA product.

2.1.2 Observations

In-situ *T* & *S* in standard levels were obtained from the World Ocean Database 23 (WOD23; Mishonov, 2024). The WOD23 aggregates global ocean observations from diverse platforms, including OSD, CTD, XBT, MBT, PFL, DRB, MRB, and GLD. WOD23 implements a well-established quality control (QC) system (Garcia et al., 2024). All observations failing to meet any of the WOD23 QC criteria were discarded. Systematic biases in XBT and MBT data were corrected according to the method of Cheng et al. (2014). Furthermore, an additional level of QC was conducted. Data were excluded where the errors relative to the background field exceeded three times the local error standard deviation (Fig. S1). This step removed ~1% of the profiles. In total, there are ~4.67×10^6 temperature and ~4.32×10^6 salinity profiles used in the study to conduct the objective analysis (Fig. S2).

Satellite observations comprise SST and SLA. For SST, we employed the 1/4° Daily Optimum Interpolation SST version 2.1 (DOISSTv2.1; Reynolds et al., 2007; Banzon et al., 2016; Huang et al., 2021) dataset. For SLA, we employed the CMEMS AVISO Level-4 SLA product, which is the same dataset as that used to generate the climatological background field. The horizontal resolution of this product is 1/8°. To improve computational efficiency, the SLA observations were remapped onto the WOA23 horizontal grid.

https://doi.org/10.5194/essd-2026-261
Preprint. Discussion started: 28 April 2026

2.1.3 Independent products for evaluation and comparison

The ARMOR3D is a global 3D *T* & *S* product with a horizontal resolution of 1/4°, covering depths from 0 to 5500 m (Guinehut et al., 2012). ARMOR3D generates fine-scale *T* & *S* structures using multivariate linear regression based on historical statistical relationships. In this study, the multi-year reprocessed weekly data in ARMOR3D were used.

The GLORYS12V4 (hereinafter referred to as GLORYS) product (Lellouche et al., 2021) is a global eddy-resolving ocean reanalysis with a horizontal resolution of 1/12°, spanning depths from 0.5 m to 5728 m. In our study, the reprocessed daily data covering 2005–2021 were applied. In subsequent evaluations, these datasets were subsampled to a weekly frequency in order to align with the 4D-MGA product.

2.2 Reconstruction Methods

2.2.1 4D-MGA

Our reconstruction method adapts the 4D-MGA framework of Wu et al. (2026b). By introducing the Laplace operator ($\mathbf{S}$), 4D-MGA can simultaneously define the spatiotemporal correlation of ocean variables. The 4D-MGA is aimed at addressing the analysis increments ($\tilde{\mathbf{X}}$) relative to the background field ($\mathbf{X}^b$). The cost function is

$$J(\tilde{\mathbf{X}}) = \frac{1}{2}\tilde{\mathbf{X}}^T[\boldsymbol{\alpha}\mathbf{S}]\tilde{\mathbf{X}} + \frac{1}{2}\left[\mathbf{H}\left(\mathbf{X}^b + \tilde{\mathbf{X}}\right) - \mathbf{Y}^{obs}\right]^T \mathbf{O}^{-1}\left[\mathbf{H}\left(\mathbf{X}^b + \tilde{\mathbf{X}}\right) - \mathbf{Y}^{obs}\right]. \tag{1}$$

Where the first term on the right-hand side is the smoothing term based on the Laplace operator ($\mathbf{S}$), $\boldsymbol{\alpha}$ is the penalty coefficient matrix to define the weight of the smoothing term; the second term is the observation term, where $\mathbf{Y}^{obs}$ represents the observations, $\mathbf{H}$ represents the linear projection operator from the background to the observations, and $\mathbf{O}^{-1}$ is the diagonal inverse matrix with elements of independent observation errors.

In Eq. (1), the smoothing term defines the continuity of error evolution, which still represents static spatiotemporal correlations. The MGA method (Li et al., 2008, 2013; Han et al., 2011, 2013) is therefore employed to enable multi-scale analysis. MGA allows for the extraction of observational signals sequentially from coarse to fine resolutions. After applying Eq. (1) on the current grid layer, the analysis results will be projected onto the finer grid by grid-doubling. As shown in Fig. 1, the coarse grid layers extract a smoothed large-scale signal from observations, while the fine grid layers complement the small-scale structures. By summing the analysis fields from each layer, the final mapping result ($\mathbf{X}^a$) is obtained:

$$\mathbf{X}^a = \mathbf{X}^b + \sum_{n=N_{start}}^{N_{end}} \mathbf{P}^{(n)}\tilde{\mathbf{X}}^{(n)}. \tag{2}$$

Where N_{start} and N_{end} are the first and last layers of the grid, respectively; $\mathbf{P}^{(n)}$ is the projection matrix interpolated from the nth layer grid to the background grid, and $\tilde{\mathbf{X}}^{(n)}$ is the increment of the observation relative to the background at the nth layer. However, in regions with sparse observations, the coarse grid layers may generate unrealistically long-range correlations. A pseudo-observation scheme is therefore introduced to constrain this effect, with its specific configuration following Wu et al. (2026b).

https://doi.org/10.5194/essd-2026-261
Preprint. Discussion started: 28 April 2026

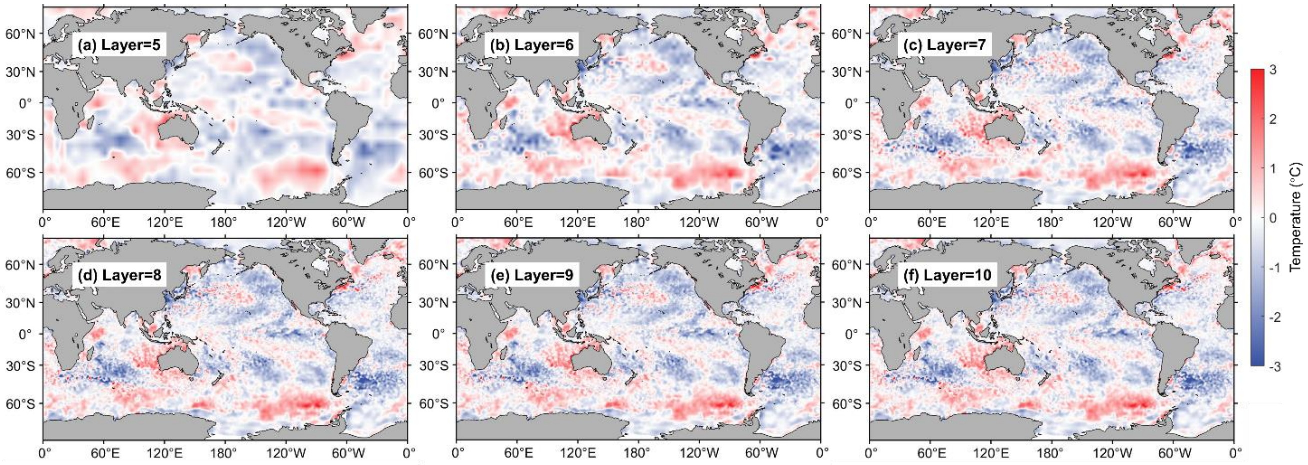

Figure 1 A diagram of the 4D-MGA adjustment for SST. (a-e) represent the results after applying 4D-MGA on the 5th to 10th layers.

2.2.2 Dynamic height integration

In the 4D-MGA framework, SLA observations will be combined with *T*/*S* observations. SLA will be approximated as the dynamic height anomaly (DHA). Since high-frequency barotropic signals induced by wind forcing and the inverse-barometer effect have been removed in the Level-4 SLA product, the barotropic component can be neglected. Through dynamic height integration, a direct relationship between T & S and the perturbation in DHA (denoted as δDHA) can then be established as follows:

$$\delta DHA = -\int_0^{z_m} \frac{\rho(P,T,S)-\rho(P,T^b,S^b)}{\rho(P,T^b,S^b)}\,dz. \tag{3}$$

Where ρ is the seawater density; $z_m = 1500\ m$ is the reference depth. If the water depth is less than z_m, the SLA observations at that grid point are not considered; T^b and S^b are background fields of T & S, respectively. $P = \rho_0 gz$ is the approximate pressure, where g (9.8 m s^{-2}) is the gravitational acceleration and ρ_0 (1025 kg m^{-3}) denotes the reference density.

By incorporating Eq. (3), the observation term for a single SLA observation can be derived:

$$OBS(\tilde{\boldsymbol{T}},\tilde{\boldsymbol{S}}) = \frac{1}{2}\left[\boldsymbol{H}\delta DHA\left(\boldsymbol{T}^b+\tilde{\boldsymbol{T}},\boldsymbol{S}^b+\tilde{\boldsymbol{S}},\boldsymbol{T}^b,\boldsymbol{S}^b\right)-\delta Y_{sla}\right]^T$$

$$O^{-1}\left[\boldsymbol{H}\delta DHA\left(\boldsymbol{T}^b+\tilde{\boldsymbol{T}},\boldsymbol{S}^b+\tilde{\boldsymbol{S}},\boldsymbol{T}^b,\boldsymbol{S}^b\right)-\delta Y_{sla}\right]. \tag{4}$$

Where $\tilde{\mathbf{T}}$ and $\tilde{\mathbf{S}}$ represent the increments of the background field of T & S from the surface to z_m, respectively; Y_{sla} is the observations of SLA and O is the observation error.

Note that Eq. (4) characterizes an underdetermined mapping between SLA observations and the full-depth vertical T & S profiles. During the minimization process, the solver tends to adjust the DHA via the highest-gradient elements, specifically S at deep layers. To mitigate this inconsistency with physical reality, $\boldsymbol{\alpha}$ is prescribed based on the variable and vertical resolution (Wu et al., 2026b).

2.3 Production of the weekly data

As shown in Equation (1), the 4D-MGA method generates four-dimensional analysis increments relative to the background fields. Following the approach of Zhou et al., (2023) and Wu et al. (2026b), the central time increments are selected to reconstruct the analysis field. In this study, the minimization time window (MTW) was set to 120 days. The MGA was performed sequentially from a horizontal resolution of ~7° (with 3 vertical layers and 2 temporal layers) to a resolution of ~1/4° (with 33 vertical layers and 5 temporal layers distributed over the MTW). For satellite observations, whose data density is sufficient, only observations at the analysis time were combined. A weekly analysis was conducted from January 1, 2005, to December 30, 2023, yielding a total of 992 reconstructions.

2.4 RMSE, bias and ACC

To estimate the performance of 4D-MGA, we introduce the root mean square error (RMSE), bias, and anomaly correlation coefficient (ACC) as validation metrics, with their respective formulas given as follows:

$$RMSE = \sqrt{\frac{1}{n}\sum_{i=1}^{n}(X_i - Y_i)^2}, \tag{5}$$

$$bias = \frac{1}{n}\sum_{i=1}^{n}(X_i - Y_i), \tag{6}$$

$$ACC = \frac{cov(\widetilde{\mathbf{X}},\widetilde{\mathbf{Y}})}{\sigma(\widetilde{\mathbf{X}})\sigma(\widetilde{\mathbf{Y}})}. \tag{7}$$

Where X_i denotes the gridded dataset and Y_i is the reference observation, with $\widetilde{\mathbf{X}}, \widetilde{\mathbf{Y}}$ representing their respective anomalies. Here, cov stands for covariance and σ is the standard deviation.

2.5 Calculation of the geostrophic currents

The geostrophic currents are estimated by using the thermal wind relation referenced to the 1500 m level:

$$\begin{cases} u_g(x,y,z) = \frac{g}{f\rho_0}\int_{z=1500\,m}^{z}\frac{\partial}{\partial y}\rho(x,y,z)dz \\ v_g(x,y,z) = -\frac{g}{f\rho_0}\int_{z=1500\,m}^{z}\frac{\partial}{\partial x}\rho(x,y,z)dz \end{cases}. \tag{8}$$

Where $u_g(x,y,z)$ and $v_g(x,y,z)$ are the zonal and meridional geostrophic velocity components, respectively; f is the Coriolis parameter; and x, y, z denote the zonal, meridional, and vertical coordinates, respectively.

3 Validation

3.1 *T* & *S*

To evaluate the overall reconstruction performance, we first compare the RMSE of the 4D-MGA product with ARMOR3D and GLORYS, using WOD23 observations as the reference. Figure 2 shows the spatially binned RMSE of *T* & *S* for the three products.

The RMSE of 4D-MGA is shown to be significantly lower or comparable to that in GLORYS and ARMOR3D. Globally averaged *T/S* RMSE values are 0.29 °C/0.09 psu, 0.49 °C/0.14 psu, and 0.29 °C/0.04 psu for ARMOR3D, GLORYS, and 4D-MGA, respectively. Regions of higher errors (*T/S* RMSE >1 °C/0.2 psu) are primarily located in the WBCs, the equatorial zone, and the Antarctic Circumpolar Current, where active multi-scale dynamics are prevalent (e.g., Figs. 5–6 below). Furthermore, the relatively large errors are manifested in the marginal seas, coastal ocean and high latitudes, which are presumably associated with the relatively sparse observations in these regions (e.g., Fig. 10 below). In terms of extreme errors, the percentage of grid points with *T/S* RMSE exceeding 0.5 °C/0.1 psu is 7%/15% for ARMOR3D, 32%/28% for GLORYS, and 9%/3% for 4D-MGA.

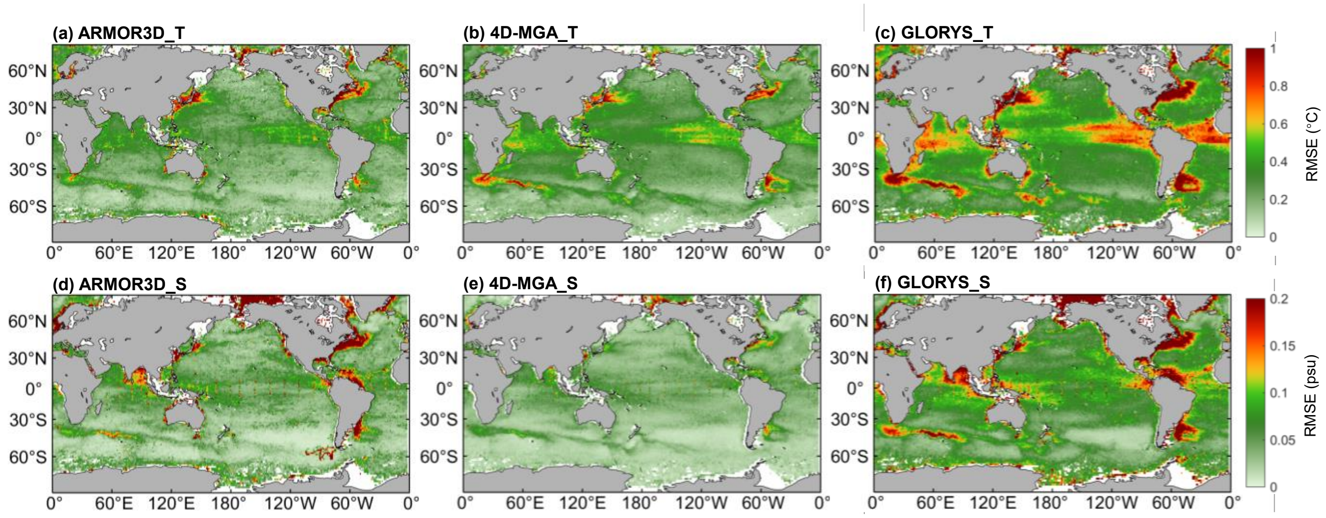

Figure 2. Spatial distribution of the 1°×1° gridded mean RMSE from 2005 to 2023 for ARMOR3D temperature (a), 4D-MGA temperature (b), and GLORYS temperature (c). (d)–(f) are the same as (a–c), but for salinity.

The vertical structure of the error is further examined. As shown in Fig. 3a, 4D-MGA achieves a lower average *T* RMSE than all other products across almost all vertical layers. The maximum *T* RMSE in the vertical are 1.12 °C (WOA23), 0.69 °C (ARMOR3D), 0.85 °C (GLORYS), and 0.55 °C (4D-MGA). For *S* (Fig. 3b), 4D-MGA holds a clear advantage in the upper ocean (<600 m). Its maximum RMSE is 0.14 psu, which is significantly smaller than others (≥0.30 psu).

The favourable RMSE performance of 4D-MGA in Figs. 3a and 3b can be largely attributed to its exceptional bias control (Figs. 3c and 3d). The coarse-resolution grid layers of 4D-MGA are sufficiently constrained by the available observational resolution, allowing them to converge robustly while filtering out small-scale random noise.

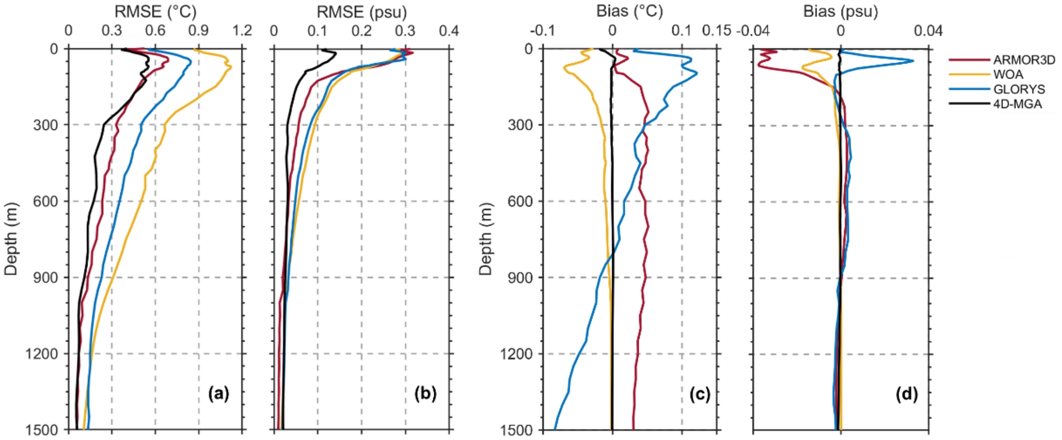

Figure 3. Full-period (2005–2023) horizontal averages of RMSE (a, b) and bias (c, d) for temperature (a, c) and salinity (b, d) from ARMOR3D, WOA23, GLORYS, and 4D-MGA.

3.2 Dynamic height anomaly

Based on the gridded *T* & *S*, we further validate the performance of DHA from the 4D-MGA product. A case from 10 August 2013 was randomly selected and is shown in Fig. 4a–4d. The distribution of DHA in 4D-MGA agrees well with the SLA in satellite observations. Both show the enrich mesoscale information (e.g., eddies, meanders and fronts etc.) with alternating positive and negative SLA in the WBCs and the Antarctic Circumpolar Current (Figs. 4a–4b). In addition, it can be seen that the RMSE of DHA remains below 0.05 m in most regions. The relatively large (>0.1 m) RMSEs appear in marginal seas, WBCs, Antarctic Circumpolar Current, and high latitudes (Fig. 4c), consistent with that in Fig. 2. At the same time, the ACC exceeds 0.6 over nearly in the global ocean (Fig. 4d), with consistency distribution with that of RMSE.

The timeseries of the DHA is also evaluated (Fig. 4e–4g). As shown in Fig. 4e–4f, 4D-MGA exhibits a significantly lower RMSE with a time-averaged value of 0.04 m (0.06 m in GLORYS and 0.05 m in ARMOR3D), and a higher ACC (time-averaged value of 0.89) over the entire period, compared with those of the GLORYS (time-averaged ACC of 0.76) and ARMOR3D (time-averaged ACC of 0.81). It is consistent with the relatively larger RMSE of GLORYS and ARMOR3D shown in Fig. 3. After 2014, an increase in RMSE alongside stronger temporal fluctuations appears, which coincides with variability of SLA (Fig. S3). This may be related to progressive upgrades in the SLA product's data fusion algorithms and the expanding constellation of altimeter missions (Pujol et al., 2016; Taburet et al., 2019).

The timeseries of the spatially averaged DHA estimated by the three products and SLA in satellite observations show the pronounced interannual signals (Fig. 4g). Their distinct correlations (r=0.99, P<0.01 for 4DMGA; r=0.79, P<0.01 for ARMOR3D; r=0.91, P<0.01 for GLORYS) with satellite observation show the advantage of the 4DMGA product. In addition, the spatially averaged DHA of ARMOR3D and GLORYS significantly exceeds SLA about 2~3 cm before 2015. This is probably because their relatively large *T* & *S* biases (Fig. 3c–3d) lead to a systematic overestimation. In contrast, 4D-MGA's DHA agrees well with the SLA, showing the reliability of the 4D-MGA product.

https://doi.org/10.5194/essd-2026-261
Preprint. Discussion started: 28 April 2026

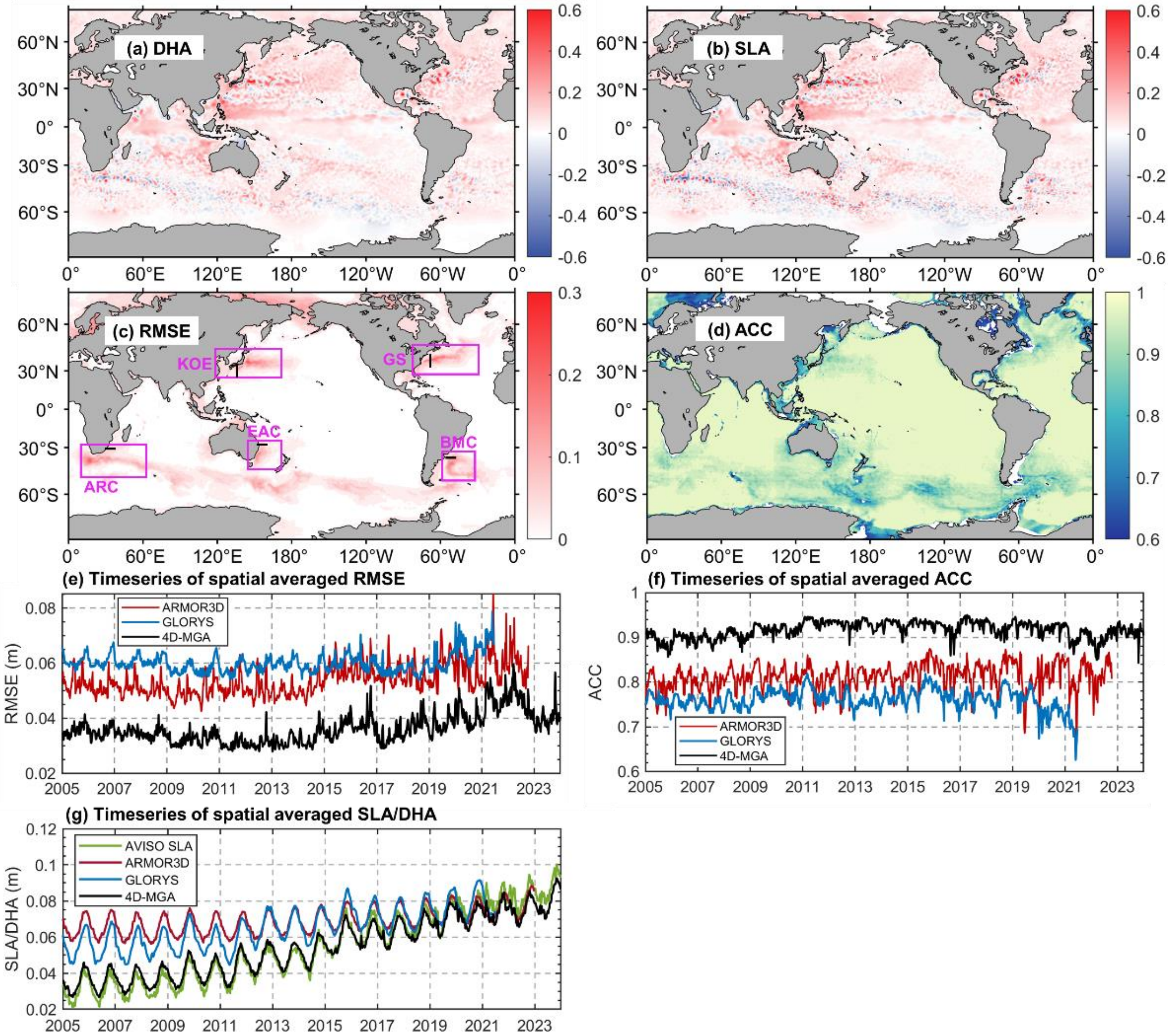

Figure 4. Spatial distribution of DHA (m) from the 4D-MGA product (a) and SLA observations (m) (b) on 10 August 2013. (c, d) Time-averaged RMSE (c) and ACC (d) of 4D-MGA DHA against SLA observations. The pink boxes in (c) indicate the major WBC regions: Kuroshio Extension (KOE), Gulf Stream (GS), Agulhas Current (ARC), East Australia Current (EAC), and Brazil Current (BMC). The black lines denote the WBC sections shown in Figs. 7–8. (e–g) Timeseries of spatially averaged RMSE (e), ACC (f), and SLA (AVISO) and DHA (ARMOR3D, GLORYS, and 4D-MGA) (g).

3.3 Geostrophic currents

The surface geostrophic currents in WBC regions (the Kuroshio, the Gulf Stream, the Agulhas Current, the East Australia Current (EAC) and Brazil Current) for August 2013 are further evaluated (Figs. 5–6). It is evident that all of the products display the significant features of WBCs with the magnitude of the geostrophic current exceeding 0.5 m s^{-1}. The location, width

https://doi.org/10.5194/essd-2026-261
Preprint. Discussion started: 28 April 2026

and intensity of the WBCs are generally consistent with each other. Furthermore, the meanders, mesoscale eddies, and fronts with horizontal scale of 25~200 km are enriched in these regions, indicating the presence of active meso-scale dynamic features. Their structures and scales are also in line with SLA observations. For example, one mesoscale eddy is located at 32°N, 145°E in the south of the Kuroshio Extension in the 4D-MGA product (Fig. 5a). This eddy has a similar intensity (~0.9 m s^{-1}) and radius (~100 km) to those in the SLA observations (Fig. 5j). It is evident that the surface geostrophic current speeds estimated by the three products are smaller than those in satellite observations. One possible cause is the assumption of a motionless plane at 1500 m. However, the spatial patterns and magnitudes of the geostrophic current speeds demonstrate a high degree of agreement, despite the presence of certain discrepancies in detail. These discrepancies in WBCs are further quantified and compared with each other, with the time-averaged ACC/RMSE values of 0.80/0.14 m s^{-1} for ARMOR3D, 0.66/0.18 m s^{-1} for GLORYS, and 0.73/0.18 m s^{-1} for 4D-MGA (Fig. 6i–j).

As demonstrated in Fig. 7, the main axis of the WBCs at the selected positions can be well captured from surface to deep ocean (>1000 m), with their maximal (minimal) velocities of 0.54 m s^{-1}, 0.63 m s^{-1}, -0.23 m s^{-1}, -0.21 m s^{-1}, -0.22 m s^{-1}, respectively. In addition, the key recirculation features in the WBCs can be adequately exhibited. For instance, the Kuroshio Counter Current (Fig. 7a), the southern recirculation of the Gulf Stream (Fig. 7b), the northward parts of the Agulhas anticyclonic circulation (Fig. 7c), and the northward recirculation of the EAC and Brazil Current (Figs. 7d–e). The location, structure and intensity of these recirculation have been shown to be consistent with previous findings (e.g., Imawaki et al., 2013; Sloyan et al., 2016; Zilberman et al., 2018; Chidichimo et al., 2021; Kawakami et al., 2022; Guo et al., 2024). Li H. et al. (2025a) provided a comprehensive analysis of the recirculation features observed in WBCs, and these features cannot be captured by the low horizontal resolution (~1°) data. In addition, the timeseries of globally averaged geostrophic currents in the vertical are further investigated, with all products in good agreement with each other (Fig. S4).

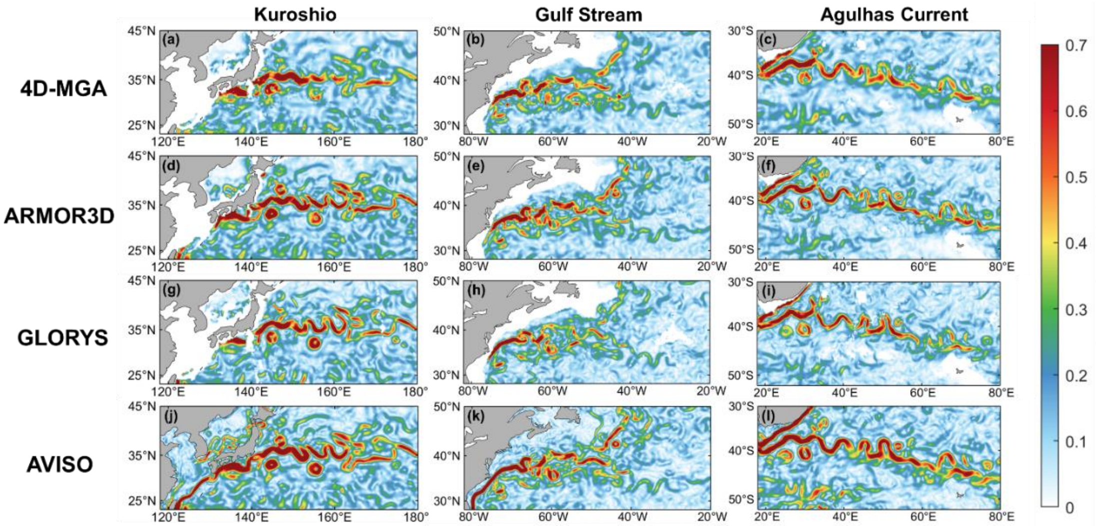

Figure 5. Spatial distribution of geostrophic current speed in selected WBC regions in August 2013. The weekly geostrophic currents from (a–c) 4D-MGA, (d–f) ARMOR3D, (g–i) GLORYS and (j–l) AVISO are each weighted and averaged to form the monthly mean fields.

https://doi.org/10.5194/essd-2026-261
Preprint. Discussion started: 28 April 2026

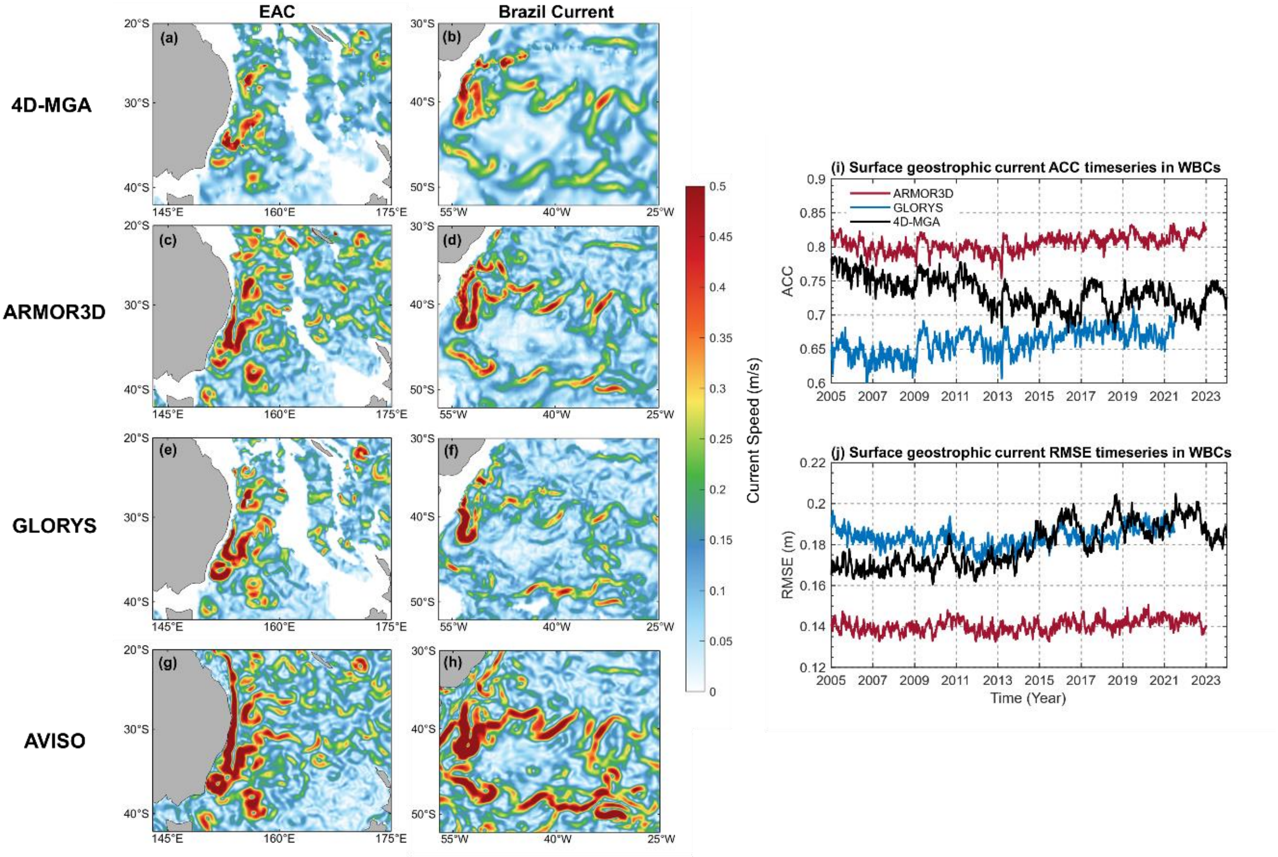

Figure 6 (a–h) Same as Fig. 5, but for the EAC and BMC. (i, j) Timeseries of spatially averaged ACC (i) and RMSE (j) for surface geostrophic currents in the WBCs against AVISO.

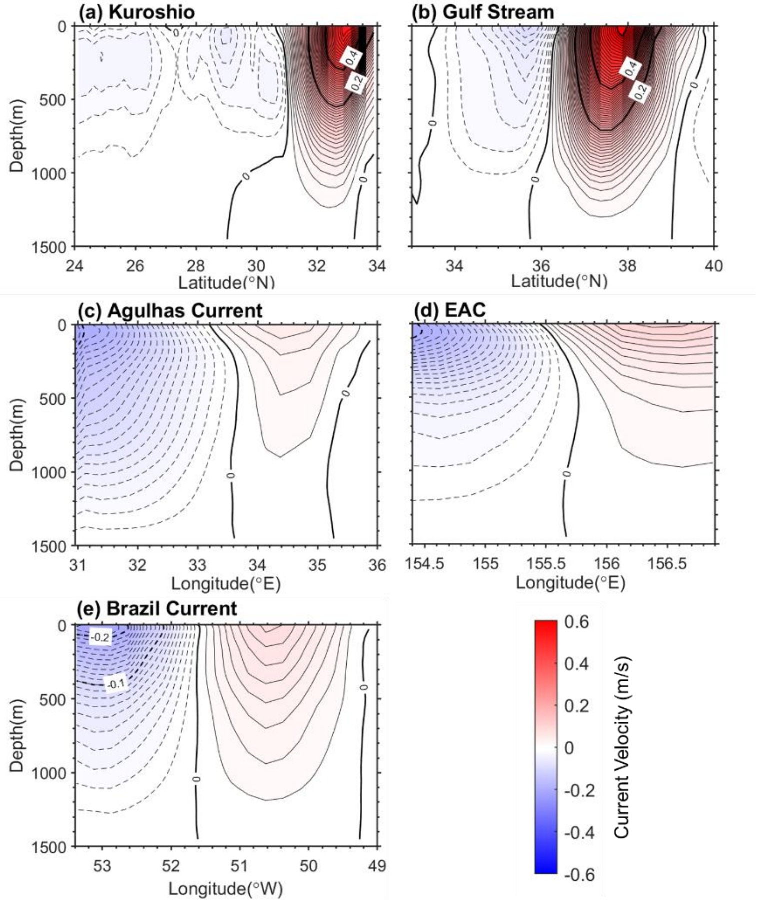

Figure 7. Climatological (2005-2023) geographic velocity sections in WBC sections from the 4D-MGA product. The contour interval is 0.01 m/s of the Kuroshio (a) at 137°E, the Gulf Stream (b) at 68.5°W, the Agulhas Current (c) at 31°S, the EAC (d) at 27°S and the Brazil Current (e) at 37°S. The positive values in (a) and (b) represent the eastward currents, while they represent the northward currents in (c), (d) and (e).

4 The linear trends of geostrophic transports in WBCs

According to the geostrophic currents at each section in Fig. 8, the timeseries of the corresponding geostrophic transports can be estimated (Fig. 9). The linear trends of the geostrophic transports in WBCs vary with region. The northward geostrophic transport of the Kuroshio at 137°E and southward geostrophic transport of Agulhas Current at 31°S exhibit a marked and consistent decrease, with a trend of 0.37 ± 0.06/0.17±0.06, 0.23 ± 0.05/0.10±0.06, 0.30 ± 0.06/0.12±0.05 Sv (1 Sv = 10^6 m^3 s^{-1}) per year in 4D-MGA, ARMOR3D, GLORYS products, respectively. The decreasing trend of the Kuroshio transports has been demonstrated in previous studies (e.g., Chandler et al., 2022; Guo et al., 2023), although it seems to be inconsistent with that in climate models (e.g., Yang et al., 2016; Chen et al., 2019). In contrast, trends for the geostrophic transports in other WBCs show less consistency across different products. In the Gulf Stream at 68.5°W, 4D-MGA product indicates a significant ($P<0.01$) positive trend of 0.39 ± 0.05 Sv per year, while other products show the negative trends. Chi et al. (2021) have reported a slight increasing trend of the surface geostrophic transports of the Gulf Stream at the similar location during 1993 to 2018. Due to the reduction of the Atlantic Meridional Overturning Circulation (e.g., Yang et al., 2016; Weijer et al., 2020), the Gulf Stream was weakened over the past decades (Piecuch and Beal, 2023). Our estimated increase in Gulf Stream transport should be further investigated. The EAC at 27.5°S shows a pronounced decrease trend of southward geostrophic transport for the 4D-MGA product, with a decrease of 0.13 ± 0.04 Sv per year. On the other hand, the Brazil Current shows nonsignificant trend of decrease of geostrophic transport for the 4D-MGA product. However, it shows an interesting interannual variability, which is probably linked to ENSO and wind stress curl as reported by De Paula et al. (2025).

Notably, our geostrophic transport estimates and trends discussed in the WBCs are probably contingent on the selected sections. Despite the presence of discrepancies among the estimates for different products, there is a high degree of consistency in their interannual variability. The correlation coefficient of the geostrophic transport between different products ranges from 0.86 to 0.88 for the Kuroshio, from 0.54 to 0.55 for the Gulf Stream, from 0.65 to 0.82 for the Agulhas Current, from 0.77 to 0.84 for the EAC, from 0.67 to 0.83 for the Brazil Current at the selected sections in our study (Fig. 8f). This demonstrates consistency among the products.

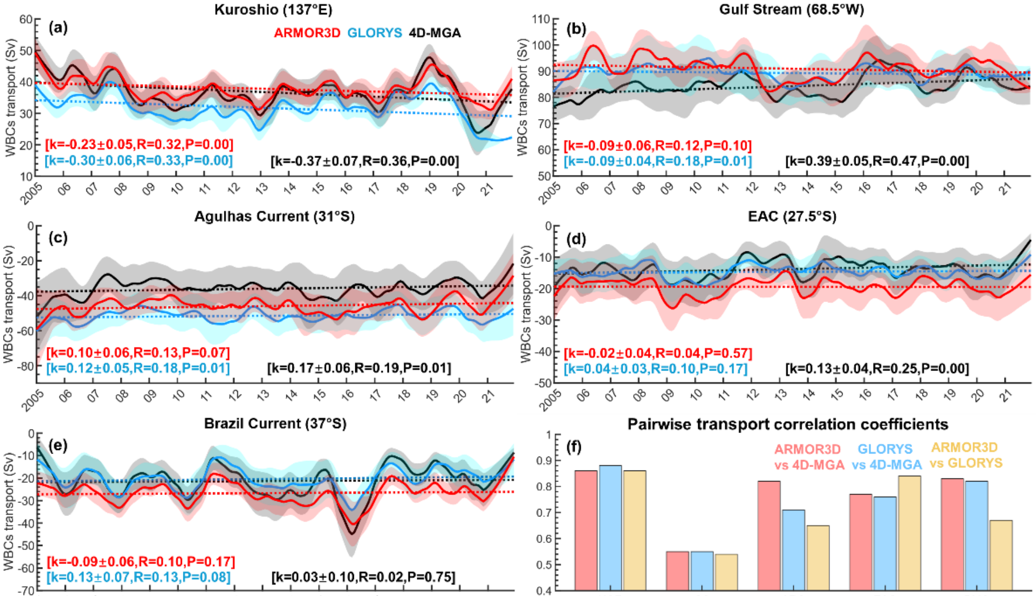

Figure 8. (a–e) Timeseries of the geostrophic transport in WBC sections. Northward and eastward velocities are defined as positive. The solid lines denote the monthly mean, the shaded areas ±1 standard deviation, and the dashed lines the linear trend. The parameters k, R and P denote the slope of the linear trend (in Sv per year, with standard error), the linear correlation coefficient between the linear trend and the mean anomaly, and the significance level (p-value) of the linear trend, respectively. (f) Pairwise correlation coefficients of the monthly mean geostrophic transport.

5 Data availability

The 4D-MGA product is freely available at https://doi.org/10.5281/zenodo.19378150 (Wu et al., 2026a) Here we provide a global ocean temperature and salinity gridded product at 1/4° resolution on 57 vertical levels from 0–1500m and at a weekly resolution from 2005 to 2023.

6 Discussion

6.1 The independent test

Our preceding assessments have validated the *T* & *S* against the WOD23, which was used for reconstruction. Hence, the generalization performance of the 4D-MGA method remains to be verified for further assessing the product's reliability. By randomly sampling 30% and 60% of the in-situ profiles in each MTW, we conducted independent tests for all analysis time steps in January, April, July, and October of the years 2005, 2014, and 2023 (54 groups in total) (Fig. 9).

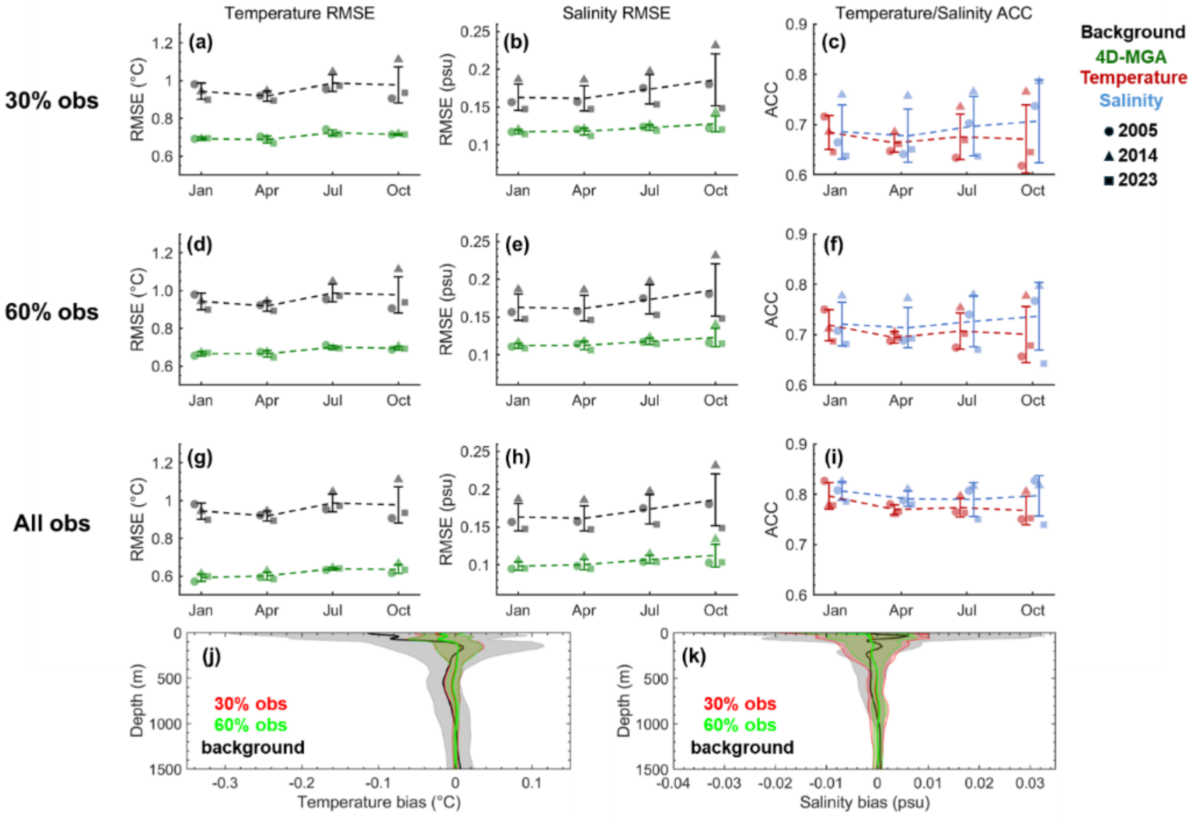

Figure 9. (a)–(i) RMSE and ACC from independent tests. Error bars indicate ±1 standard deviation. Dashed lines represent the mean value across independent test groups. Circles, triangles, and squares denote the annual mean values for the years 2005, 2014, and 2023, respectively. (a–c) 30% assimilated vs. 70% validated; (d–f) 60% vs. 40%; (g–i) 100% vs. 100% (non-independent). (j, k) Vertical profiles of *T* & *S* bias from the independent tests are compared against the bias of the background field. The solid line indicates the mean bias, and the shaded area represents ±1 standard deviation.

The results show 4D-MGA's excellent robustness. The method can effectively extract core dynamic signals from both small subsets and data-rich environments. Even with only 30% of the in-situ observations, the ACC for *T* & *S* still exceeds 0.6, and the averaged RMSEs for *T* & *S* are small than 0.8 °C and 0.15 psu, respectively. Conversely, in 2014, observational density 300 increased markedly in dynamically active regions (Fig. 10). While the strong random fluctuations lead to the worst RMSE performance of the background, 2014 achieves the highest ACC after assimilation. Moreover, the minimal standard deviations of the assimilated ACC and RMSE further demonstrate the good stability of the 4D-MGA method. Complementing this robustness, the substantially reduced mean and standard deviation of the systematic bias further validate its excellent bias-correction capability (Fig. 9j–k).

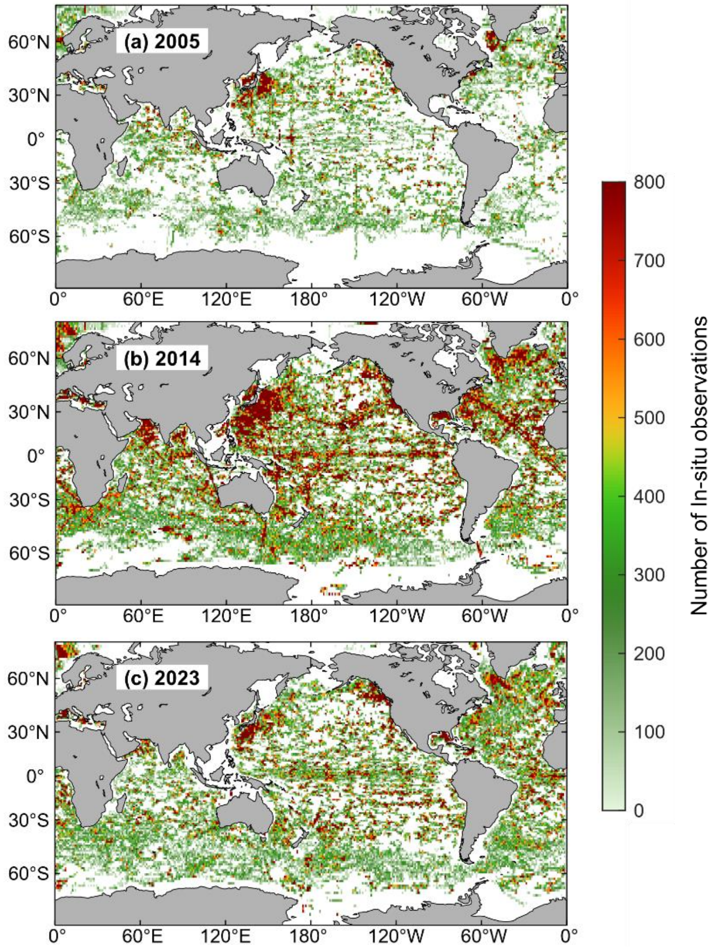

305

Figure 10. Spatial distribution of the annual number of 1°×1° in-situ observations for 2005, 2014, and 2023.

6.2 Deficiencies and future improvements

While the 4D-MGA method and product demonstrate significant advantages and robust performance, the current analysis framework has several notable limitations. First, 4D-MGA is inherently less sensitive to nonlinear error evolution. Specifically, the limited number of temporal grid layers may not only filter out resolvable signals but also introduce additional noise. Second, despite the inclusion of additional background constraints, the dynamic height integration process may still lead to distorted adjustments in deep layers. Third, the approximation of DHA by SLA can introduce potential errors owing to the neglect of barotropic signals.

To address these limitations, several potential avenues are worth exploring in future research: (1) Parallelize the minimizer to overcome array-size constraints. This would achieve a higher effective time resolution and better capture nonlinear evolutions. (2) Refine the spatial scale and weighting of SLA observations based on local in-situ data density to enhance the product's determinism. (3) The idea of incorporating bottom pressure data to separate barotropic and baroclinic signals has been proposed (Li Z. et al., 2025b). Although existing pressure products are limited by their accuracy and resolution (Schindelegger et al., 2021; Chen et al., 2023; Yang et al., 2025), coupling such an approach with in-situ constraints could further improve the accuracy of the dynamic height integration framework.

7 Conclusion

This study produced a weekly 1/4° global subsurface *T* & *S* gridded dataset during 2005 to 2023 using the 4D-MGA method. Without prior statistical assumptions, the 4D-MGA efficiently extracts observational information via four-dimensional multi-scale analysis and physical constraints from dynamic height integration. Spatiotemporal correlations and multi-variable observational constraints enable the resolution of both large- and mesoscale structures. The results demonstrate that the 4D-MGA product performs well in several areas:

(1) High accuracies. The 4D-MGA product achieves the remarkably low RMSE across almost all regions and depths relative to WOD23. On average, the 4D-MGA product has a *T/S* RMSE of 0.29 °C/0.04 psu, which is smaller than the ARMOR3D and GLORYS products.

(2) Excellent ability to capture mesoscale information. Compared with the time-series of the eddy-resolved SLA in satellite observations, the global averaged DHA estimated by the 4D-MGA *T* & *S* gridded data set has a much lower RMSE, higher ACC and higher correlation coefficients (RMSE=0.04 m; ACC=0.89; r=0.99, P<0.01). It is slightly better than that of the GLORYS (RMSE=0.06 m; ACC=0.76; r=0.91, P<0.01) and the ARMOR3D (RMSE=0.05 m; ACC=0.81; r=0.79, P<0.01). Moreover, the WBC structures (like eddies and recirculation) can also be accurately represented. This capability is further evidenced by its successful capture of long-term trends and interannual variability in WBC transports.

In summary, the 4D-MGA product provides a high-fidelity objective analysis dataset with considerable value for further understanding the oceanic mesoscale processes and climate change.

Author contributions

H. W. generated and evaluated the 4D-MGA product. H. W., W. L., G. Z. and H. Y. L. developed the related algorithm. W. L. conceptualized and supervised this study. H. L. and G. H. edited and revised the manuscript. L. C. and Q. Z. participated in data processing and sample selection.

Competing interests

The contact author has declared that none of the authors has any competing interests.

References

Argo: Argo float data and metadata from Global Data Assembly Centre (Argo GDAC), https://doi.org/10.17882/42182, 2026.

AVISO/DUACS: SWOT Level-3 KaRIn Low Rate SSH Expert (3.0), https://doi.org/10.24400/527896/A01-2023.018, 2024.

Bagnell, A. and DeVries, T.: 20th century cooling of the deep ocean contributed to delayed acceleration of Earth's energy imbalance, Nat. Commun., 12, 4604, https://doi.org/10.1038/s41467-021-24472-3, 2021.

Banzon, V., Smith, T. M., Chin, T. M., Liu, C., and Hankins, W.: A long-term record of blended satellite and in situ sea-surface temperature for climate monitoring, modeling and environmental studies, Earth Syst. Sci. Data, 8, 165–176, https://doi.org/10.5194/essd-8-165-2016, 2016.

Cao, L., Li, W., Zhang, Y., Han, G., Qin, Y., Liang, K., Wang, X., Li, H., Zhou, G., Wu, H., Zheng, Q., He, J., Tong, Y., and Zhang, Y.: MOHDAS: MaCOM Operational Hybrid Data Assimilation System Based on the Analytical 4-Dimensional Ensemble Variational Method, Ocean-Land-Atmos Res., 5, 0135, https://doi.org/10.34133/olar.0135, 2026.

Carton, J. A., Penny, S. G., and Kalnay, E.: Temperature and Salinity Variability in the SODA3, ECCO4r3, and ORAS5 Ocean Reanalyses, 1993–2015, J. Clim., 32, 2277–2293, https://doi.org/10.1175/JCLI-D-18-0605.1, 2019.

Castillo-Trujillo, A. C., Kwon, Y.-O., Fratantoni, P., Chen, K., Seo, H., Alexander, M. A., and Saba, V. S.: An evaluation of eight global ocean reanalyses for the Northeast U.S. Continental shelf, Prog. Oceanogr., 219, 103126, https://doi.org/10.1016/j.pocean.2023.103126, 2023.

Chamberlain, M. A., Oke, P. R., Fiedler, R. A. S., Beggs, H. M., Brassington, G. B., and Divakaran, P.: Next generation of Bluelink ocean reanalysis with multiscale data assimilation: BRAN2020, Earth Syst. Sci. Data, 13, 5663–5688, https://doi.org/10.5194/essd-13-5663-2021, 2021.

Chandler, M., Zilberman, N. V., and Sprintall, J.: Seasonal to Decadal Western Boundary Current Variability From Sustained Ocean Observations, Geophys. Res. Lett., 49, e2022GL097834, https://doi.org/10.1029/2022GL097834, 2022.

Chang, Y.-S., Vecchi, G. A., Rosati, A., Zhang, S., and Yang, X.: Comparison of global objective analyzed T-S fields of the upper ocean for 2008–2011, J. Mar. Syst., 137, 13–20, https://doi.org/10.1016/j.jmarsys.2014.04.001, 2014.

Chen, C., Wang, G., Xie, S.-P., and Liu, W.: Why Does Global Warming Weaken the Gulf Stream but Intensify the Kuroshio?, J. Clim., 32, 7437–7451, https://doi.org/10.1175/JCLI-D-18-0895.1, 2019.

Chen, L., Yang, J., and Wu, L.: Topography Effects on the Seasonal Variability of Ocean Bottom Pressure in the North Pacific Ocean, J. Phys. Oceanogr., 53, 929–941, https://doi.org/10.1175/JPO-D-22-0140.1, 2023.

Cheng, L. and Zhu, J.: Benefits of CMIP5 Multimodel Ensemble in Reconstructing Historical Ocean Subsurface Temperature Variations, J. Clim., 29, 5393–5416, https://doi.org/10.1175/JCLI-D-15-0730.1, 2016.

Cheng, L., Zhu, J., Cowley, R., Boyer, T., and Wijffels, S.: Time, Probe Type, and Temperature Variable Bias Corrections to Historical Expendable Bathythermograph Observations, J. Atmos. Oceanic Technol., 31, 1793–1825, https://doi.org/10.1175/JTECH-D-13-00197.1, 2014.

Chepurin, G. A., Carton, J. A., Sun, L., and Penny, S. G.: SODA4: a mesoscale ocean/sea ice reanalysis 1980–2024, Earth Syst. Sci. Data Discuss. [preprint], https://doi.org/10.5194/egusphere-2025-3810, 1 October 2025.

Chi, L., Wolfe, C. L. P., and Hameed, S.: Has the Gulf Stream Slowed or Shifted in the Altimetry Era?, Geophysical Research Letters, 48, e2021GL093113, https://doi.org/10.1029/2021GL093113, 2021.

Chidichimo, M. P., Piola, A. R., Meinen, C. S., Perez, R. C., Campos, E. J. D., Dong, S., Lumpkin, R., and Garzoli, S. L.: Brazil Current Volume Transport Variability During 2009–2015 From a Long-Term Moored Array at 34.5°S, JGR Oceans, 126, e2020JC017146, https://doi.org/10.1029/2020JC017146, 2021.

De Boisseson, E., Zuo, H., Chrust, M., Browne, P., Balmaseda, M., and De Rosnay, P.: ECMWF 6th generation ocean and sea-ice reanalysis system (ORAS6), EGU General Assembly 2024, Vienna, Austria, 14–19 Apr 2024, EGU24-10659, https://doi.org/10.5194/egusphere-egu24-10659, 2024.

De Paula, T. P., Arruda, W. Z., Lima, J. A. M., Daher, V. B., and Violante-Carvalho, N.: Spatial and temporal variability of the Brazil current path: Diagnostics from satellite-derived altimetry and a global reanalysis product, Deep-Sea Res. Pt. I, 219, 104474, https://doi.org/10.1016/j.dsr.2025.104474, 2025.

Donlon, C. J., Martin, M., Stark, J., Roberts-Jones, J., Fiedler, E., and Wimmer, W.: The Operational Sea Surface Temperature and Sea Ice Analysis (OSTIA) system, Remote Sens. Environ., 116, 140–158, https://doi.org/10.1016/j.rse.2010.10.017, 2012.

El Aouni, A., Gaudel, Q., Regnier, C., Van Gennip, S., Le Galloudec, O., Drevillon, M., Drillet, Y., and Lellouche, J.: GLONET: Mercator's End-to-End Neural Global Ocean Forecasting System, JGR: Machine Learning and Computation, 2, e2025JH000686, https://doi.org/10.1029/2025JH000686, 2025.

Forget, G., Campin, J.-M., Heimbach, P., Hill, C. N., Ponte, R. M., and Wunsch, C.: ECCO version 4: an integrated framework for non-linear inverse modeling and global ocean state estimation, Geosci. Model Dev., 8, 3071–3104, https://doi.org/10.5194/gmd-8-3071-2015, 2015.

Gaillard, F., Reynaud, T., Thierry, V., Kolodziejczyk, N., and Von Schuckmann, K.: In Situ–Based Reanalysis of the Global Ocean Temperature and Salinity with ISAS: Variability of the Heat Content and Steric Height, J. Clim., 29, 1305–1323, https://doi.org/10.1175/JCLI-D-15-0028.1, 2016.

Garcia, H. E., Boyer, T. P., Locarnini, R. A., Reagan, J. R., Mishonov, A. V., Baranova, O. K., Paver, C. R., Wang, Z., Bouchard, C., Cross, S., Seidov, D., and Dukhovskoy, D.: World Ocean Database 2023 User's Manual, NOAA atlas NESDIS ; 98, https://doi.org/10.25923/J8GQ-EE82, 2024.

Good, S. A., Martin, M. J., and Rayner, N. A.: EN4: Quality controlled ocean temperature and salinity profiles and monthly objective analyses with uncertainty estimates, JGR Oceans, 118, 6704–6716, https://doi.org/10.1002/2013JC009067, 2013.

Gray, A. R. and Riser, S. C.: A method for multiscale optimal analysis with application to A rgo data, JGR Oceans, 120, 4340–4356, https://doi.org/10.1002/2014JC010208, 2015.

Gray, P., Boss, E., Prochaska, X., Kerner, H., Demeaux, C., and Lehahn, Y.: The Promise and Pitfalls of Machine Learning in Ocean Remote Sensing, Oceanog., 37, https://doi.org/10.5670/oceanog.2024.511, 2024.

Guinehut, S., Dhomps, A.-L., Larnicol, G., and Le Traon, P.-Y.: High resolution 3-D temperature and salinity fields derived from in situ and satellite observations, Ocean Sci., 8, 845–857, https://doi.org/10.5194/os-8-845-2012, 2012.

Guo, H., Chen, Z., Yang, H., Long, Y., Zhu, R., Zhang, Y., Jing, Z., and Yang, C.: Estimating the Volume Transport of Kuroshio Extension Based on Satellite Altimetry and Hydrographic Data, J. Atmos. Oceanic Technol., 40, 1105–1118, https://doi.org/10.1175/JTECH-D-23-0018.1, 2023.

Guo, X., Yang, X., Deng, Q., Lin, H., and Wang, D.: Rhythms of the Agulhas Current Within the Framework of Energetic Anisotropy, JGR Oceans, 129, e2024JC021044, https://doi.org/10.1029/2024JC021044, 2024.

Han, G., Li, W., Zhang, X., Li, D., He, Z., Wang, X., Wu, X., Yu, T., and Ma, J.: A regional ocean reanalysis system for coastal waters of China and adjacent seas, Adv. Atmos. Sci., 28, 682–690, https://doi.org/10.1007/s00376-010-9184-2, 2011.

Han, G., Fu, H., Zhang, X., Li, W., Wu, X., Wang, X., and Zhang, L.: A global ocean reanalysis product in the China Ocean Reanalysis (CORA) project, Adv. Atmos. Sci., 30, 1621–1631, https://doi.org/10.1007/s00376-013-2198-9, 2013.

Huang, B., Liu, C., Banzon, V., Freeman, E., Graham, G., Hankins, B., Smith, T., and Zhang, H.-M.: Improvements of the Daily Optimum Interpolation Sea Surface Temperature (DOISST) Version 2.1, J. Clim., 34, 2923–2939, https://doi.org/10.1175/JCLI-D-20-0166.1, 2021.

Imawaki, S., Bower, A. S., Beal, L., and Qiu, B.: Western Boundary Currents, in: International Geophysics, vol. 103, Elsevier, 305–338, https://doi.org/10.1016/B978-0-12-391851-2.00013-1, 2013.

Ishii, M., Fukuda, Y., Hirahara, S., Yasui, S., Suzuki, T., and Sato, K.: Accuracy of Global Upper Ocean Heat Content Estimation Expected from Present Observational Data Sets, SOLA, 13, 163–167, https://doi.org/10.2151/sola.2017-030, 2017.

Kawakami, Y., Kojima, A., Murakami, K., Nakano, T., and Sugimoto, S.: Temporal variations of net Kuroshio transport based on a repeated hydrographic section along 137°E, Clim Dyn, 59, 1703–1713, https://doi.org/10.1007/s00382-021-06061-8, 2022.

Lellouche, J.-M., Eric, G., Romain, B.-B., Gilles, G., Angélique, M., Marie, D., Clément, B., Mathieu, H., Olivier, L. G., Charly, R., Tony, C., Charles-Emmanuel, T., Florent, G., Giovanni, R., Mounir, B., Yann, D., and Pierre-Yves, L. T.: The Copernicus Global 1/12° Oceanic and Sea Ice GLORYS12 Reanalysis, Front. Earth Sci., 9, 698876, https://doi.org/10.3389/feart.2021.698876, 2021.

Li, H., Xu, F., Zhou, W., Wang, D., Wright, J. S., Liu, Z., and Lin, Y.: Development of a global gridded Argo data set with Barnes successive corrections: A NEW GLOBAL GRIDDED ARGO DATA SET, J. Geophys. Res. Oceans, 122, 866–889, https://doi.org/10.1002/2016JC012285, 2017.

Li, H., Xu, F., and Wang, G.: Global Mapping of Mesoscale Eddy Vertical Tilt, JGR Oceans, 127, e2022JC019131, https://doi.org/10.1029/2022JC019131, 2022.

Li, H., Wang, G., Xu, F., Cheng, L., Li, J., Zhang, L., Wang, Y., Li, W., Yu, H., Liu, Z., and Li, Z.: Representation of western boundary currents under different climatologies with varying horizontal resolutions, https://doi.org/10.22541/essoar.174188285.57160751/v1, 13 March 2025a.

Li, W., Xie, Y., He, Z., Han, G., Liu, K., Ma, J., and Li, D.: Application of the Multigrid Data Assimilation Scheme to the China Seas' Temperature Forecast, Journal of Atmospheric and Oceanic Technology, 25, 2106–2116, https://doi.org/10.1175/2008JTECHO510.1, 2008.

Li, W., Xie, Y., and Han, G.: A theoretical study of the multigrid three-dimensional variational data assimilation scheme using a simple bilinear interpolation algorithm, Acta Oceanol. Sin., 32, 80–87, https://doi.org/10.1007/s13131-013-0292-6, 2013.

Li, Z., Fei, J., Zhang, R., Jiang, X., Ma, W., Cheng, X., Liu, L., Wang, G., and Chen, C.: Numerical prediction of oceanic mesoscale circulation and satellite altimetry data assimilation in the Western Pacific, Sci. China Earth Sci., 68, 909–927, https://doi.org/10.1007/s11430-024-1488-1, 2025b.

Liang, X., Liu, C., Ponte, R. M., and Chambers, D. P.: A Comparison of the Variability and Changes in Global Ocean Heat Content from Multiple Objective Analysis Products During the Argo Period, Journal of Climate, 1–47, https://doi.org/10.1175/JCLI-D-20-0794.1, 2021.

Liu, X., Feng, L., Cheng, L., Tan, Z., Sui, C., and Song, C.: Spatiotemporal Changes of Ocean Heat Content in the Seas around China, Adv. Atmos. Sci., https://doi.org/10.1007/s00376-025-5018-0, 2026.

Lyman, J. M. and Johnson, G. C.: Estimating Global Ocean Heat Content Changes in the Upper 1800 m since 1950 and the Influence of Climatology Choice*, Journal of Climate, 27, 1945–1957, https://doi.org/10.1175/JCLI-D-12-00752.1, 2014.

Mason, E., Ruiz, S., Bourdalle-Badie, R., Reffray, G., García-Sotillo, M., and Pascual, A.: New insight into 3-D mesoscale eddy properties from CMEMS operational models in the western Mediterranean, Ocean Sci., 15, 1111–1131, https://doi.org/10.5194/os-15-1111-2019, 2019.

Matei, D., Pohlmann, H., Jungclaus, J., Müller, W., Haak, H., and Marotzke, J.: Two Tales of Initializing Decadal Climate Prediction Experiments with the ECHAM5/MPI-OM Model, Journal of Climate, 25, 8502–8523, https://doi.org/10.1175/JCLI-D-11-00633.1, 2012.

Mishonov, A. V.: World Ocean Database 2023, NOAA atlas NESDIS ; 97, https://doi.org/10.25923/Z885-H264, 2024.

Miyaji, Y., Kido, S., Tomita, H., and Tanimoto, Y.: Mesoscale eddy influence on North Pacific air–sea heat exchange in a high-resolution ocean reanalysis, J Oceanogr, 81, 505–514, https://doi.org/10.1007/s10872-025-00767-7, 2025.

Nunziante, G., Storto, A., and Yang, C.: Systematic error correction in numerical ocean models with artificial neural networks, , https://doi.org/10.5194/egusphere-egu25-19733, 2025.

Pan, Y., Cheng, L., Abraham, J., Trenberth, K. E., Reagan, J., Du, J., Wang, Z., Storto, A., Von Schuckmann, K., Zhu, Y., Mann, M. E., Zhu, J., Wang, F., Yu, F., Locarnini, R., Fasullo, J., Huang, B., Graham, G., Yin, X., Gouretski, V., Zheng, F., Li, Y., Zhang, B., Wan, L., Chen, X., Wang, D., Feng, L., Song, X., Liu, Y., Reseghetti, F., Simoncelli, S., Chen, G., Zhang, R., Mishonov, A., Wei, W., Tan, Z., Li, G., Cao, L., Chen, L., Yuan, H., Lyu, K., Sulaiman, A., Mayer, M., Wang, H., Ma, Z., Bao, S., Yan, H., Liu, Z., Yang, C., Liu, X., Hausfather, Z., Gues, F., Song, X., Zhang, M., and Chen, L.: Ocean Heat Content Sets Another Record in 2025, Adv. Atmos. Sci., https://doi.org/10.1007/s00376-026-5876-0, 2026.

Paris, C. B., Cowen, R. K., Lwiza, K. M. M., Wang, D.-P., and Olson, D. B.: Multivariate objective analysis of the coastal circulation of Barbados, West Indies: implication for larval transport, Deep Sea Research Part I: Oceanographic Research Papers, 49, 1363–1386, https://doi.org/10.1016/S0967-0637(02)00033-X, 2002.

Paul, A., Maheswaran, P. A., Satheesan, K., and Kottayil, A.: Assessing ocean reanalysis accuracy for marine extremes in the Indian ocean using in-situ observations, Clim Dyn, 63, 343, https://doi.org/10.1007/s00382-025-07780-y, 2025.

Piecuch, C. G. and Beal, L. M.: Robust Weakening of the Gulf Stream During the Past Four Decades Observed in the Florida Straits, Geophysical Research Letters, 50, e2023GL105170, https://doi.org/10.1029/2023GL105170, 2023.

Polkova, I., Swingedouw, D., Hermanson, L., Köhl, A., Stammer, D., Smith, D., Kröger, J., Bethke, I., Yang, X., Zhang, L., Nicolì, D., Athanasiadis, P. J., Karami, M. P., Pankatz, K., Pohlmann, H., Wu, B., Bilbao, R., Ortega, P., Yang, S., Sospedra-Alfonso, R., Merryfield, W., Kataoka, T., Tatebe, H., Imada, Y., Ishii, M., and Matear, R. J.: Initialization shock in the ocean circulation reduces skill in decadal predictions of the North Atlantic subpolar gyre, Front. Clim., 5, 1273770, https://doi.org/10.3389/fclim.2023.1273770, 2023.

Pujol, M.-I., Faugère, Y., Taburet, G., Dupuy, S., Pelloquin, C., Ablain, M., and Picot, N.: DUACS DT2014: the new multi-mission altimeter data set reprocessed over 20years, Ocean Sci., 12, 1067–1090, https://doi.org/10.5194/os-12-1067-2016, 2016.

Reagan, J. R., Boyer, T. P., Garcia, H. E., Locarnini, R. A., Baranova, O. K., Bouchard, C., Cross, S. L., Mishonov, A. V., Paver, C. R., Seidov, D., Wang, Z., and Dukhovskoy, D.: World Ocean Atlas 2023, 2024a.

Reagan, J. R., Seidov, D., Wang, Z., Dukhovskoy, D., Boyer, T. P., Locarnini, R. A., Baranova, O. K., Mishonov, A. V., Garcia, H. E., Bouchard, C., Cross, S. L., and Paver, C. R.: World Ocean Atlas 2023, Volume 2: Salinity, NOAA Atlas NESDIS ; 90, https://doi.org/10.25923/70QT-9574, 2024b.

Reynolds, R. W., Smith, T. M., Liu, C., Chelton, D. B., Casey, K. S., and Schlax, M. G.: Daily High-Resolution-Blended Analyses for Sea Surface Temperature, Journal of Climate, 20, 5473–5496, https://doi.org/10.1175/2007JCLI1824.1, 2007.

Roemmich, D. and Gilson, J.: The 2004–2008 mean and annual cycle of temperature, salinity, and steric height in the global ocean from the Argo Program, Progress in Oceanography, 82, 81–100, https://doi.org/10.1016/j.pocean.2009.03.004, 2009.

Schindelegger, M., Harker, A. A., Ponte, R. M., Dobslaw, H., and Salstein, D. A.: Convergence of Daily GRACE Solutions and Models of Submonthly Ocean Bottom Pressure Variability, JGR Oceans, 126, e2020JC017031, https://doi.org/10.1029/2020JC017031, 2021.

Schneider, D. P., Deser, C., Fasullo, J., and Trenberth, K. E.: Climate Data Guide Spurs Discovery and Understanding, EoS Transactions, 94, 121–122, https://doi.org/10.1002/2013EO130001, 2013.

Sloyan, B. M., Ridgway, K. R., and Cowley, R.: The East Australian Current and Property Transport at 27°S from 2012 to 2013, Journal of Physical Oceanography, 46, 993–1008, https://doi.org/10.1175/JPO-D-15-0052.1, 2016.

Su, H., Zhang, H., Geng, X., Qin, T., Lu, W., and Yan, X.-H.: OPEN: A New Estimation of Global Ocean Heat Content for Upper 2000 Meters from Remote Sensing Data, Remote Sensing, 12, 2294, https://doi.org/10.3390/rs12142294, 2020.

Szekely, T.: In-Situ TAC OA products: INSITU GLO_PHY_TS_OA_MY_013_052. Issue 1.12., Copernicus Marine Environmental Monitoring Service (CMEMS), 16 pp., https://doi.org/https://doi.org/10.25607/OBP-1972, 2022.

Taburet, G., Sanchez-Roman, A., Ballarotta, M., Pujol, M.-I., Legeais, J.-F., Fournier, F., Faugere, Y., and Dibarboure, G.: DUACS DT2018: 25 years of reprocessed sea level altimetry products, Ocean Sci., 15, 1207–1224, https://doi.org/10.5194/os-15-1207-2019, 2019.

Talley, L. D., Pickard, G. L., Emery, W. J., and Swift, J. H.: Introduction to Descriptive Physical Oceanography, in: Descriptive Physical Oceanography, Elsevier, 1–6, https://doi.org/10.1016/B978-0-7506-4552-2.10001-0, 2011.

Tan, Z., Cheng, L., Gouretski, V., Zhang, B., Wang, Y., Li, F., Liu, Z., and Zhu, J.: A new automatic quality control system for ocean profile observations and impact on ocean warming estimate, Deep Sea Research Part I: Oceanographic Research Papers, 194, 103961, https://doi.org/10.1016/j.dsr.2022.103961, 2023.

Tan, Z., Zhu, Y., Cheng, L., Gouretski, V., Pan, Y., Yuan, H., Wang, Z., Li, G., Song, X., Zhang, B., Bao, S., Li, Y., and Zhu, J.: CODC-S: A quality-controlled global ocean salinity profiles dataset, Sci Data, 12, 917, https://doi.org/10.1038/s41597-025-05172-9, 2025.

Tang, Y., Kleeman, R., Moore, A. M., Weaver, A., and Vialard, J.: The use of ocean reanalysis products to initialize ENSO predictions, Geophysical Research Letters, 30, 2003GL017664, https://doi.org/10.1029/2003GL017664, 2003.

Tian, T., Cheng, L., Wang, G., Abraham, J., Wei, W., Ren, S., Zhu, J., Song, J., and Leng, H.: Reconstructing ocean subsurface salinity at high resolution using a machine learning approach, Earth Syst. Sci. Data, 14, 5037–5060, https://doi.org/10.5194/essd-14-5037-2022, 2022.

Wang, H., Zhang, L., Yang, S., Yan, X., and Li, Z.: Attention Enhanced 3D-U-Net++ Ocean Temperature and Salinity Reconstruction in the Northwestern Pacific based on Transfer Learning, https://doi.org/10.5194/essd-2025-742, 12 December 2025.

Weijer, W., Cheng, W., Garuba, O. A., Hu, A., and Nadiga, B. T.: CMIP6 Models Predict Significant 21st Century Decline of the Atlantic Meridional Overturning Circulation, Geophysical Research Letters, 47, e2019GL086075, https://doi.org/10.1029/2019GL086075, 2020.

Wu, H., Li, W., Li, H., Han, G., Zhou, G., Liu, H., Cao, L., and Zheng, Q.: 1/4° global temperature and salinity objective analysis using 4D-MGA (1.0), https://doi.org/10.5281/ZENODO.19378150, 2026a.

Wu, H., Li, W., Han, G., Zhang, Y., Wu, X., Cao, L., Zhou, G., Liu, H., and Zheng, Q.: The 4D-MGA multi-scale data assimilation system for the 1/12° global MaCOM, Ocean-Land-Atmos Res, olar.0146, https://doi.org/10.34133/olar.0146, 2026b.

Yang, F., Bai, J., Liu, H., Zhang, W., Wu, Y., Liu, S., Shi, C., Zhang, T., Zhong, M., Zhu, Z., Wang, C., Forootan, E., Yu, J., Yu, Z., and Xiao, Y.: CRA-LICOM: a global high-frequency atmospheric and oceanic temporal gravity field product (2002–2024), Earth Syst. Sci. Data, 17, 4691–4714, https://doi.org/10.5194/essd-17-4691-2025, 2025.

Yang, H., Lohmann, G., Wei, W., Dima, M., Ionita, M., and Liu, J.: Intensification and poleward shift of subtropical western boundary currents in a warming climate, JGR Oceans, 121, 4928–4945, https://doi.org/10.1002/2015JC011513, 2016.

Zhang, Z., Wang, W., and Qiu, B.: Oceanic mass transport by mesoscale eddies, Science, 345, 322–324, https://doi.org/10.1126/science.1252418, 2014.

Zhou, G., Han, G., Li, W., Wang, X., Wu, X., Cao, L., and Li, C.: High-Resolution Gridded Temperature and Salinity Fields From Argo Floats Based on a Spatiotemporal Four-Dimensional Multigrid Analysis Method, JGR Oceans, 128, e2022JC019386, https://doi.org/10.1029/2022JC019386, 2023.

Zhou, S., Zhang, Y., Li, H., Liu, L., Liao, E., and Xu, F.: Shoreward shift of oceanic mesoscale activity over the last three decades, Nat Commun, 16, 10381, https://doi.org/10.1038/s41467-025-65359-x, 2025.

Zhu, Q., Li, H., Sun, H., Xia, T., Wang, X., and Han, Z.: 3DV-Unet: Eddy-Resolving Reconstruction of Three-Dimensional Upper-Ocean Physical Fields from Satellite Observations, Remote Sensing, 17, 3394, https://doi.org/10.3390/rs17193394, 2025.

Zilberman, N. V., Roemmich, D. H., Gille, S. T., and Gilson, J.: Estimating the Velocity and Transport of Western Boundary Current Systems: A Case Study of the East Australian Current near Brisbane, Journal of Atmospheric and Oceanic Technology, 35, 1313–1329, https://doi.org/10.1175/JTECH-D-17-0153.1, 2018.